Fuel 291 (2021) 120141

Contents lists available at ScienceDirect

Fuel

journal homepage: www.elsevier.com/locate/fuel

Full Length Article

Hydrocarbon mixture phase behavior in multi-scale systems in relation to shale oil recovery: The effect of pore size distributions

Yinuo Zhao, Zhehui Jin *

School of Mining and Petroleum Engineering, Department of Civil and Environmental Engineering, University of Alberta, Edmonton, AB T6G 1H9, Canada

ARTICLE INFO

Keywords:
Hydrocarbon mixtures
Phase behaviors
Density functional theory
Shale
Pore size distributions
Multi-scale system

ABSTRACT

Shale media contains a large amount of nano-scale pores, with their total pore volume comparable to that of the connected macropores and natural/hydraulic fractures (bulk). Previous work largely neglected the interplay between nanopores and bulk region as well as the effect of pore size distribution (PSD), where fluids can freely exchange between nanopores and bulk region. To accurately predict production and ultimate oil recovery, PSD effect should be taken into consideration. In this work, engineering density functional theory (DFT) is used to study phase behaviors of hydrocarbon mixtures in multi-scale nanoporous media with PSD effect during constant composition expansion (CCE) and constant volume depletion (CVD) processes. We found that under the PSD effect, due to the chemical equilibrium between various nanopores and connected bulk as well as competitive adsorption in nanopores, the interplay between nanopores and bulk region influences phase behaviors and properties of fluids in the multi-scale system. Phase transitions first occur in the bulk region, then the larger pores followed by the smaller pores. The bulk bubble point pressure increases as the volume ratio of the smaller pores in the system increases, while the bulk dew point decreases. When fluids in one specific pore begin to vaporize, in other pores, the heavier component would be adsorbed, while the lighter component would be released, which suppresses the phase transitions in the smaller pores because of the heavier component accumulation. The higher volume ratio of the smaller pores suppresses the heavier component production, when pressure is below the bulk dew point.

1. Introduction

In the recent decades, the exploitation and production of unconventional oil/gas have drastically increased as the global energy consumption continuously increases and conventional reservoirs gradually deplete [1–3]. Unlike the conventional reservoirs, pores in shale formations are predominantly in nanoscale [4]. As a result, the conventional equations of state (EOS) modeling becomes inapplicable for the prediction of shale fluid properties [5–7]. On the other hand, the hydraulic and natural fractures connected to vast nano-scale pores form the recovery routes for the hydrocarbons stored in shale nanoporous matrix [8]. Since fluids can freely exchange between nanopores and macropores/fractures (the so-called interplay between nanopores and macropores/fractures), such nanopore-fracture multi-scale system in shale formations further complicates the *in-situ* fluid properties, which are multi-component and multi-phase [9,10]. As hydrocarbon mixture phase behaviors in shale media play a crucial role in the predictions of well productivity, ultimate oil recovery and the applications of enhanced oil recovery (EOR) technologies [8], it is imperative to understand the hydrocarbon mixture phase behaviors in the multi-scale systems and the interplay between nanopores and macropores/fractures.

In this regard, there have been a number of experimental measurements using indirect and direct observations to study hydrocarbon mixture phase behavior in nanoporous media. The indirect (observation) methods include using differential scanning calorimetry (DSC) [6,11] and slope change in pressure–volume plot [12–14]. While Deo and his coworkers observed that the bubble point pressures of nano-confined methane/n-decane and methane/n-octane mixtures are slightly reduced [12,14], Liu *et al.* [15] observed that the bubble point pressure of nitrogen/n-butane mixture in a crushed shale sample containing PVT cell is higher than the bulk one due to the competitive adsorption of nitrogen and n-butane in nanopores. They also indicate that the interplay between nanopores and macropores/fractures can influence the properties of hydrocarbon mixtures in multi-scale systems [15]. Besides the indirect method, the lab-on-a-chip technology can

* Corresponding author.
E-mail address: zhehui2@ualberta.ca (Z. Jin).

https://doi.org/10.1016/j.fuel.2021.120141
Received 18 October 2020; Received in revised form 29 December 2020; Accepted 4 January 2021

achieve direct observations of phase transitions of nanoconfined fluids in a near-equilibrium process. Wang *et al.* [16] found that a ternary mixture of n-butane/*iso*-butane/n-octane in nanochannels does not vaporize, even when the hydrocarbon mixtures in connected microchannels completely vaporize. Alfi *et al.* [17] used the lab-on-a-chip technology to directly visualize the phase transitions of binary hydrocarbon mixtures (pentane/hexane and pentane/heptane) and a ternary hydrocarbon mixture (pentane/hexane/heptane) in 10-nm, 50-nm and 100-nm nanochannels. They found that while the bubble point temperature of hydrocarbon mixtures in the 10-nm nanochannels increases significantly, those in the 50-nm and 100-nm nanochannels are close to the bulk. Zhong *et al.* [10] directly visualized the instantaneous phase transitions of hydrocarbon mixtures (methane/propane) in nanochannels, which are connected to microchannels. The bubble point pressure of hydrocarbon mixtures in 8-nm nanochannels is severely suppressed to be below their bulk dew point pressure and the confinement effect magnifies as pore size decreases. Although these advanced nanofluidic technologies have shed lights on hydrocarbon phase behaviors in nanopores, the interplay between nanopores and macropores/fractures inherent in shale matrix is difficult to realize due to the drastic volume difference between microchannels and nanochannels [10]. As a result, the effect of interplay between nanochannels and connected microchannels on fluid properties in the multi-scale system is negligible, while the fluids in the microchannels behave as bulk.

Underlying mechanisms of fluid phase behaviors in nanopore-facture multi-scale system have been studied from theoretical and simulation perspectives. By using a pore-size-dependent equation of state modeling (PR-C EOS), Luo *et al.* [18] found that when the pore volume of 15-nm pores and the connected bulk region are comparable at the initial condition, the bubble point pressure of oil in the bulk region is reduced. By using a modified isothermal-isobaric Gibbs ensemble Monte Carlo simulation, Bi and Nasrabadi [19] observed an increased bulk bubble point pressure P_b^{bub} of a binary hydrocarbon mixture (methane/ethane), which are connected to 4-nm pores. Recently, we used an engineering density functional theory (DFT) to study phase behaviors of methane-propane mixtures in nanopores which are connected to bulk regions [20]. We found that two-phases could coexist in nanopores, and nanopore two-phase region expands as pore size increases. However, we used a uniform pore size model, which does not consider pore size distribution (PSD) inherent in shale studies [4]. Since PSD is crucial for characterization of shale reservoirs, accurate estimation of reservoir storage, knowledge about fluid flow mechanisms and production behaviors [21–25], using a uniform pore size model may become inapplicable. Although many previous works studied pore size effect [5,26,27], a single-nanopore model is generally used and fluid behaviors in various nanopores are independent of each other. Some work [28,29] studied PSD effect without considering the interplay between nanopores and macropores/fractures. However, in shale media, various nanopores are connected with macropores/fractures, forming a complex multi-scale system, in which fluid properties are affected by their interplay [30,31].

In this regard, Wang *et al.* [32,33] used the Peng-Robinson equations of state (PR-EOS) plus capillary pressure model to study continuous phase transitions in shale nanoporous media consisting of four representative nanopores and fractures. They assumed that the phase transitions in nanopores occur at varying pressures for pores of different sizes. They further assumed that the smaller pores are saturated with liquids, while the larger pores have liquid-to-vapor phase transitions. Even though these works provided important insights into hydrocarbon phase behaviors in various nanopores connected with fractures, such EOS-based models do not consider the fluid-surface interactions and inhomogeneous density distributions under nano-confined environment. Luo *et al.* [18,34] considered fluid-surface interactions in their triple-scale PR-C EOS model, in which 5-nm and 15-nm pores are connected to fractures. They found a suppressed bulk bubble point P_b^{bub} during constant composition expansion (CCE) process. However, these works only lower the pressure to a value higher than the bulk dew point P_b^{dew} so that the information about P_b^{dew} and phase transitions as well as fluid depletions in nanopores is missing. As a result, the phase behaviors of hydrocarbon mixtures in nanopores with PSD connected with macropores/fractures are still not clear yet.

In this work, we simultaneously consider the effect of fluid-surface interaction, interplay between nanopores and macropores/fractures, and the PSD inherent in shale media to investigate phase behaviors of C_1/C_3 mixture. We use a simplified carbon slit-pore to represent the nanoconfinement effect in kerogen, which plays a dominant role in fluid-in-place in shale reservoirs [35–38]. Slit-shaped pores are widely distributed in kerogen [39,40]. Both kerogen and carbon surfaces are strongly oil wet [41–44] and carbon slit pores have been widely used to model kerogen pores in molecular simulations [45,46]. Both CCE and constant volume depletion (CVD) processes are discussed by comparing three different nanopore-fracture multi-scale systems, which consist of various nanopores of different sizes and a fracture (bulk region). While we explicitly consider the fluid-surface interactions in nanopores, the fluids in fractures are treated as bulk. Based on the multi-scale model, we study continuous phase transitions and hydrocarbon mixture recovery in various nanopores and the bulk region. This work should provide important insights into the effect of PSD and interplay between nanopores and macropores/fractures in actual shale oil production processes.

2. Methods

2.1. The Nanopores-bulk model

In this work, we construct a multi-scale system with the PSD effect in which two different nanopores of pore sizes as 5 nm and 10 nm are considered. As in our previous work [9,20], the fluids in nanopores and bulk region are in chemical equilibrium. In our previous nanofluidic measurements [10], we found that in a near-equilibrium pressure drawdown process, in which the pressure drawdown rate is set as $\sim$ 0.035 MPa/min, equivalently $\sim$ 50.4 MPa/day, C_1/C_3 vaporization dynamics and initiations can be captured by the engineering DFT which is conducted at an equilibrium state. In contrast, the pressure drawdown rate during an actual shale production is generally less than 1 MPa/day [47,48]. Therefore, we use the equilibrium pressure drawdown to convey the knowledge about the actual shale oil production process.

We use C_1/C_3 mixture to illustrate the effect of PSD on hydrocarbon mixture phase behavior in a multi-scale system. As shown in Fig. 1, three different systems are studied, in which the pore volumes of nanopores and bulk region volume ratio are given as: 1) **Case A**: $V_{5\text{nm}} : V_{10\text{nm}} : V_b^{int} = 1 : 0 : 1$; 2) **Case B**: $V_{5\text{nm}} : V_{10\text{nm}} : V_b^{int} = 0.5 : 0.5 : 1$; 3) **Case C**: $V_{5\text{nm}} : V_{10\text{nm}} : V_b^{int} = 0 : 1 : 1$, where $V_{5\text{nm}}$ and $V_{10\text{nm}}$ represent the pore volumes in 5-nm and 10-nm pores, respectively, and V_b^{int} is initial bulk volume which is comparable to the total volume of nanopores according to inherent characteristics of shale [49,50]. The nanopores are simulated as structureless carbon slit pores which is completely oil wet, while the bulk region represents macropores/fracture without confinement effect [9]. The fluid properties in the nanopores and bulk region are determined by materials balance (MB) and chemical equilibrium [20]. We use the Peng-Robinson EOS (PR-EOS) [51] to calculate bulk chemical potentials. When the bulk fluids are in a vapor–liquid coexistence phase, due to the equal chemical potentials in vapor and liquid phases, liquid phase chemical potentials are used to calculate fluid compositions in nanopores [20]. The details of DFT calculation are shown in **Supplementary Information**.

2.2. Material balance

CCE and CVD processes are simulated under an isothermal condition of $T = 288.15$ K. We specify the initial bulk region C_3 composition $y_{C_3,b}$ as 0.8 and the initial pressure P^{int} as 45 bar in all cases. We illustrate the

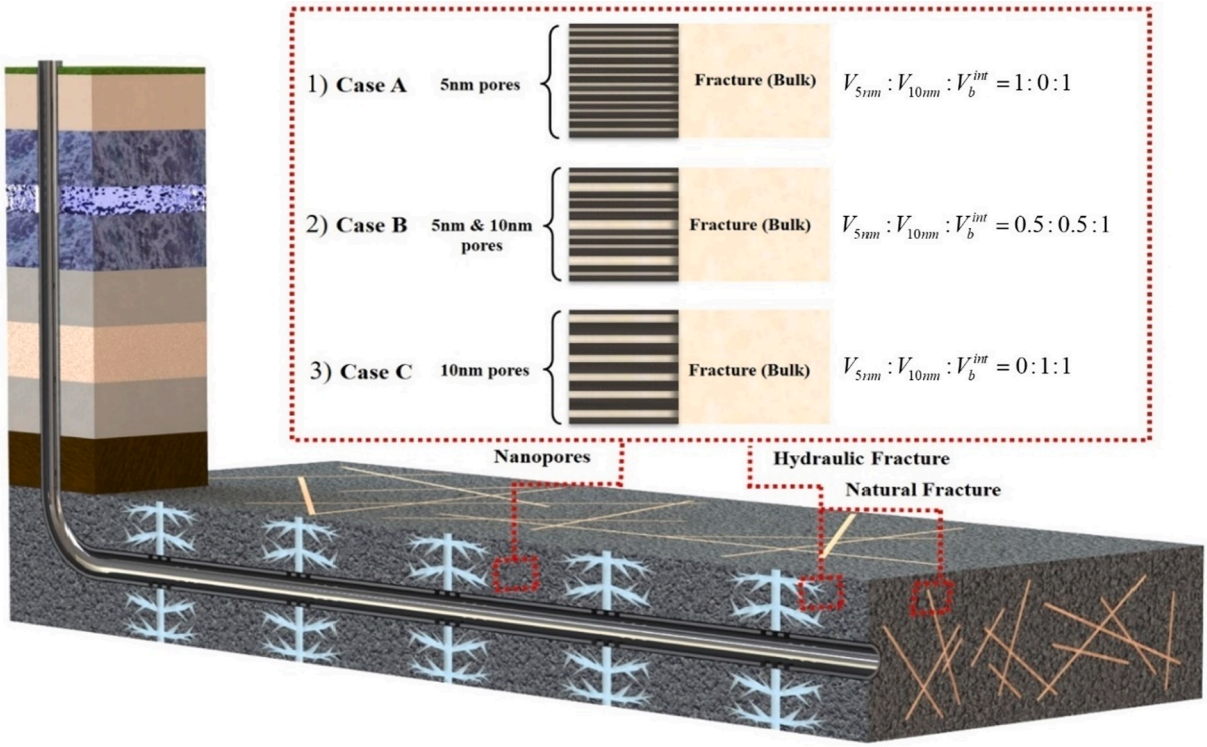

Fig. 1. Schematic representation of shale oil extraction operation, where nanopores are connected to fractures/macropores (bulk) [9]. In our work, nanopores of pore volumes V_p are connected to a bulk region of volume V_b. 1) **Case A:** $V_{5\text{nm}} : V_{10\text{nm}} : V_b^{int} = 1 : 0 : 1$; 2) **Case B:** $V_{5\text{nm}} : V_{10\text{nm}} : V_b^{int} = 0.5 : 0.5 : 1$; 3) **Case C:** $V_{5\text{nm}} : V_{10\text{nm}} : V_b^{int} = 0 : 1 : 1$.

MB calculations of the CCE and CVD processes in two separate subsections. The flowcharts of the calculation procedures for the CCE and CVD processes are shown in Figs. S1 and S2 (Supplementary Information), respectively.

2.2.1. CCE

In CCE process, as system pressure P (dictated by the bulk region pressure) decreases, the bulk region volume V_b increases, while the nanopore volumes of various sizes V_p remain constant. The total amount of hydrocarbons in the nanopores-bulk system is constant. MB calculations are illustrated in three different pressure conditions: **a)** P above the bubble point pressure in the bulk region P_b^{bub} ($P > P_b^{bub}$); **b)** P between P_b^{bub} and P_b^{dew} ($P_b^{bub} > P > P_b^{dew}$); **c)** P below P_b^{dew} ($P < P_b^{dew}$).

a) $P > P_b^{bub}$

In this case, the bulk region is in a single liquid-phase. For given $\{y_{i,b}\}$ at P, the average densities of component i in bulk, $\rho_{i,b}$ and nanopores, $\rho_{i,p}$ are obtained from the PR-EOS and DFT, respectively. The total molar number of component i at the initial condition (for a given initial pressure P^{int}), N_i^{int}, is given as,

$$N_i^{int} = \rho_{i,b}^{int} V_b^{int} + \sum \rho_{i,p}^{int} V_p,\ i = C_1, C_3,\ p = 5\text{nm}, 10\text{nm} \quad (1)$$

in which $\rho_{i,b}^{int}$ and $\rho_{i,p}^{int}$ represent the average molar densities of component i in bulk and nanopores of p at P^{int}. Note that $\{N_i^i\}$ remain constant during the CCE process. As P decreases, V_b increases, which is given as,

$$V_b = \left(N_i^{int} - \sum \rho_{i,p} V_p\right) \Big/ \rho_{i,b},\ i = C_1, C_3,\ p = 5\text{nm}, 10\text{nm} \quad (2)$$

As shown in Eq. (2), the equilibrium V_b for given P can be obtained from C_1 and C_3 MB equations. As in our previous work [20], for given P and T, by varying trial C_3 composition in the bulk region $x_{C_3,b}$, we find the intercept between two $V_b - x_{C_3,b}$ curves from C_1 and C_3 to determine the equilibrium $\{y_{i,b}\}$ as shown in **Fig. S3**. The equilibrium phase transition point determined from the grand potential (GP) minimum branch [52] is used to represent the hydrocarbon mixture behaviors. At equilibrium, GP is minimum for an open system in which the fluids in nanopores are in chemical equilibrium with those in bulk [53].

b) $P_b^{bub} > P > P_b^{dew}$

In this case, the bulk region is in a vapor–liquid coexistence phase. Unlike Eq. (1), $\{N_i^{int}\}$ are given as,

$$N_i^{int} = \rho_{i,b(L)} V_{b(L)} + \rho_{i,b(V)} V_{b(V)} + \sum \rho_{i,p} V_p,\ i = C_1, C_3,\ p = 5\text{nm}, 10\text{nm} \quad (3)$$

where $\rho_{i,b(L)}$ and $\rho_{i,b(V)}$ represent molar densities of component i in the bulk liquid and vapor phases obtained from PR-EOS, respectively; $V_{b(L)}$ and $V_{b(V)}$ are volumes of the bulk liquid and vapor phases, respectively. The bulk liquid phase chemical potentials from the PR-EOS are used as an input for DFT calculations. By rewriting Eq. (3), we have the bulk liquid volume as,

$$V_{b(L)} = \left(N_i^{int} - \sum \rho_{i,p} V_p\right) \Big/ \left[\rho_{i,b(L)} + \left(V_{b(V)}/V_{b(L)}\right)\rho_{i,b(V)}\right],\ i = C_1, C_3,\ p = 5\text{nm}, 10\text{nm}. \quad (4)$$

According to $V_{b(V)}/V_{b(L)}$ from PR-EOS, the bulk vapor volume after expansion, $V_{b(V)}$, is given as,

$$V_{b(V)} = \left(V_{b(V)}/V_{b(L)}\right)V_{b(L)} \tag{5}$$

Then, the bulk total volume after expansion is given as

$$V_b = V_{b(V)} + V_{b(L)} \tag{6}$$

As in $P > P_b^{bub}$ case, for given P and T, by varying $x_{C_3,b}$, we find the intercept between two $V_b - x_{C_3,b}$ curves from C_1 and C_3 to determine the equilibrium $\left\{y_{i,b}\right\}$ as shown in Fig. S3**a**. The highest and lowest pressures when there is an intercept between the two $V_b - x_{C_3,b}$ curves from C_1 and C_3 within bulk vapor–liquid coexist region are P_b^{bub}(see Fig. S3**b**) and P_b^{dew} (see Fig. S3**d**), respectively.

c) $P < P_b^{dew}$

In this case, the bulk region is in a single vapor-phase. When nanopores region is also in a single-phase (liquid or vapor), $\{N_i^{int}\}$ and the equilibrium V_b for given P are the same as in Eqs. (1) and (2), respectively. The equilibrium $\left\{y_{i,b}\right\}$ is determined by the intercept between two $V_b - x_{C_3,b}$ curves from C_1 and C_3 as shown in Figs. S4**a and e**.

When a specific nanopore is in a vapor–liquid coexistence phase, no intercept between $V_b - x_{C_3,b}$ curves (V_b obtained from Eq. (2)) exists as shown in Figs. S4**c** and **g**, which is due to the discontinuity in $\rho_{i,p}$. We find that for a given P, the discontinuities in $\rho_{i,p}$ in different nanopores occur at different $x_{C_3,b}$. We use the 10-nm pore as an example to illustrate. Within the 10-nm pore two-phase region, $\{N_i^{int}\}$ is given as

$$N_i^{int} = \rho_{i,b}V_b + \rho_{i,10\text{nm}(L)}V_{10\text{nm}(L)} + \rho_{i,10\text{nm}(V)}V_{10\text{nm}(V)} + \rho_{i,5\text{nm}}V_{5\text{nm}},\ i = C_1, C_3 \tag{7}$$

where $\rho_{i,10\text{nm}(L)}$ and $\rho_{i,10\text{nm}(V)}$ represent average molar densities of component i in the 10-nm pore liquid and vapor phases, respectively; $V_{10\text{nm}(L)}$ and $V_{10\text{nm}(V)}$ are volumes of the 10-nm pore liquid and vapor phases, respectively. The equilibrium $\left\{y_{i,b}\right\}$ is determined as $x_{C_3,b}$, when there is discontinuity in $V_b - x_{C_3,b}$ curves. $V_{10\text{nm}(L)}$ and $V_{10\text{nm}(V)}$ have the relationship as following,

$$V_{10\text{nm}(L)} + V_{10\text{nm}(V)} = V_{10\text{nm}} \tag{8}$$

By combining Eqs. (7) and (8), $V_{p(L)}$, $V_{p(V)}$, and V_b are given as

$$V_{10\text{nm}(V)} = \frac{N_{C_1}^{int}\rho_{C_3,b} - N_{C_3}^{int}\rho_{C_1,b} - \rho_{C_1,10\text{nm}(L)}\rho_{C_3,b}V_{10\text{nm}} + \rho_{C_3,10nm(L)}\rho_{C_1,b}V_{10\text{nm}} - \rho_{C_1,5\text{nm}}\rho_{C_3,b}V_{5\text{nm}} + \rho_{C_3,5\text{nm}}\rho_{C_1,b}V_{5\text{nm}}}{\left(\rho_{C_1,10\text{nm}(V)} - \rho_{C_1,10\text{nm}(L)}\right)\rho_{C_3,b} - \left(\rho_{C_3,10nm(V)} - \rho_{C_3,10\text{nm}(L)}\right)\rho_{C_1,b}}$$

$$V_{10\text{nm}(L)} = V_{10\text{nm}} - V_{10\text{nm}(V)} \tag{10}$$

$$V_b = \left(N_i^{int} - \rho_{i,10\text{nm}(L)}V_{10\text{nm}(L)} - \rho_{i,10\text{nm}(V)}V_{10\text{nm}(V)} - \rho_{i,5\text{nm}}V_{5\text{nm}}\right)/\rho_{i,b}, i = C_1, C_3 \tag{11}$$

The highest pressure when there is an intercept between the two $V_b - x_{C_3,b}$ curves from C_1 and C_3 within 10-nm pore phase transition region is the bubble point in 10-nm pores $P_{10\text{nm}}^{bub}$ as shown in Fig. S4**b**, while the lowest pressure is the dew point $P_{10\text{nm}}^{dew}$ as shown in Fig. S4**d**. When phase transitions occur in 5-nm nanopores, the fluids in 10-nm pores are in single vapor phase, and the bubble point and dew point in 5-nm nanopores, $P_{5\text{nm}}^{bub}$ and $P_{5\text{nm}}^{dew}$, can be obtained by applying the same method as shown in Figs. S4**f** and **h**.

2.2.2. CVD

During a CVD process, after V_b increases as P decreases, the fluids in the expanded bulk volume are depleted from the nanopores-bulk multiscale system and V_b recovers to V_b^{int} [33]. Note that 1 bar is used as the pressure gradient in our CVD calculation. The MB calculations under different pressure conditions are the same as those in CCE process. The only difference is the extra volume depletion process followed by the bulk volume expansion for each pressure drop process. The corresponding volume depletion is illustrated below.

a) $P > P_b^{bub}$

In this case, for each pressure drawdown, the expanded bulk volume at equilibrium condition could be obtained by Eq. (2), then the depleted volume V_b^d is given as,

$$V_b^d = V_b - V_b^{int} \tag{12}$$

The produced fluids from the system N_i^d and remaining fluids in the system N_i^r are given as,

$$N_i^d = \rho_{i,b}V_b^d \tag{13}$$

$$N_i^r = N_i^{int} - N_i^d \tag{14}$$

For the next pressure condition, the N_i^r would be the new N_i^{int}

b) $P_b^{bub} > P > P_b^{dew}$

When the bulk fluids split into vapor–liquid two phases, the expanded bulk volume can be obtained from Eqs. (4)-(6). We assume that only the bulk vapor phase is depleted, considering that vapor phase viscosity is much lower than that of the liquid phase [54]. Then, the depleted vapor phase volume is given as

$$V_{b(V)}^d = V_b - V_b^{int} \tag{15}$$

The produced fluids from the system N_i^d and remaining fluids in the system N_i^r are given as,

$$N_i^d = \rho_{i,b(V)}V_{b(V)}^d \tag{16}$$

$$N_i^r = N_i^{int} - N_i^d \tag{17}$$

where $\rho_{i,b(V)}$ represents densities of component i in the bulk vapor phase obtained from the PR-EOS. For the next pressure condition, the N_i^r would be the new N_i^{int}.

c) $P < P_b^{dew}$

In this case, hydrocarbons in the bulk region is in a single vapor-phase. After obtaining equilibrium expanded bulk volume according to (9)-(11), the depleted volume V_b^d, produced fluids from system N_i^d and remaining fluids in the system N_i^r can be calculated from Eqs. (12)-(14).

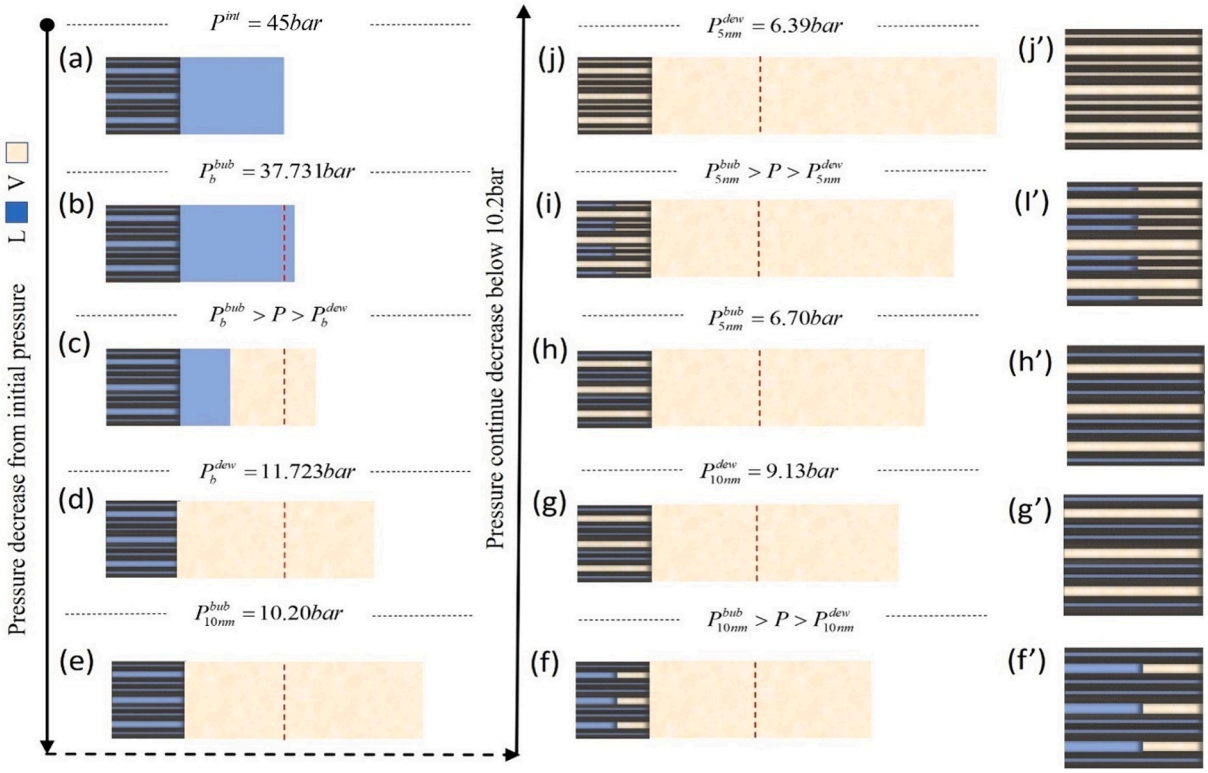

Fig. 2. The schematic diagram for phase transitions in **Case B** during the CCE process at 288.15 K. (a) P^{int} = 45bar; (b) P_b^{bub} = 37.731bar; (c)$P_b^{dew} > P > P_{10nm}^{bub}$; (d) P_b^{dew} = 11.723bar; (e)P_{10nm}^{bub} = 10.20bar; (f) $P_{10nm}^{bub} > P > P_{10nm}^{dew}$; (g) P_{10nm}^{dew} = 9.13bar; (h) P_{5nm}^{bub} = 6.7bar; (i) $P_{5nm}^{bub} > P > P_{5nm}^{dew}$; (j) P_{5nm}^{dew} = 6.39bar. (f'); (g'); (h'); (i') and (j') are enlarged parts for nanopores in (f); (g); (h); (i) and (j), respectively. The blue color represents C_1/C_3 mixture in liquid phase while the yellow color represents vapor phase in nanopores or bulk region. The red dashed line provides a reference for the volume of bulk at initial condition. (For interpretation of the references to color in this figure legend, the reader is referred to the web version of this article.)

3. Results and discussions

Both CCE and CVD methods have been widely used to study hydrocarbon mixture phase behaviors [55]. In CCE process, the system pressure is lowered stepwise by incrementally expanding the volume of outside bulk. The phase behaviors and properties of fluids in nanopores vary as the connected bulk volume expansion. The CVD process mimic the real production process by depleting the fluids in the excess bulk volume at each pressure step. In this section, we first investigate phase behaviors and fluid properties in the nanopore-bulk multi-scale system for the CCE process, then we conduct the CVD process. Finally, the PSD effect on bubble point and dew point in nanopores-bulk multi-scale system is discussed.

3.1. CCE

In Fig. 2, we present the schematic diagram for phase transitions in **Case B** during the CCE process at 288.15 K. At initial condition of P^{int} = 45 bar, C_1/C_3 mixture in the whole multi-scale system is in pure liquid phase as shown in Fig. 2**a**. After pressure decreases to be below bulk bubble point pressure P_b^{bub}, C_1/C_3 mixture in the bulk region split into vapor and liquid two phases while those in the nanopores remain as liquid phase as shown in Fig. 2**c**. It is because the competitive adsorption enhances the composition of heavier component in nanopores as we will discuss later. Note that the competitive adsorption in this work refers to the competition between the light and heavy components in nanopores. After fluids in bulk region completely vaporize, phase transitions happen in 10-nm pores firstly as shown in Fig. 2**f**. Only after fluids in the 10-nm pores completely vaporize, phase transition could occur in the 5-nm pores as shown in Fig. 2**i**. This is not only because of the stronger confinement effect in the smaller pores, but also the heavier component

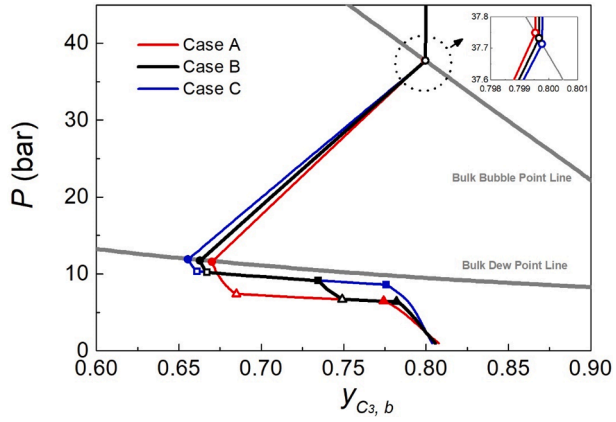

Fig. 3. The equilibrium $y_{C_3,b}$ for **Case A**, **B**, and **C** during the CCE process. The open circles represent P_b^{bub}, the solid circles represent P_b^{dew}, the open squares represent P_{10nm}^{bub}, the solid squares represent P_{10nm}^{dew}, the open triangles represent P_{5nm}^{bub}, and the solid triangles represent P_{5nm}^{dew}.

accumulation induced by interplay between nanopores and bulk. Overall, the phase transitions in the multi-scale system with PSD effect following the sequence of bulk, larger pores and small pores as pressure decreases. This phenomenon is in line with the experimental work by Wang *et al.* [16,33] and the gauge-GCMC molecular simulation results [28].

The equilibrium $y_{C_3,b}$ for different cases are presented in Fig. 3. The equilibrium $y_{C_3,b}$ varies as P decreases, which is in line with the field observation [56]. At initial condition of P^{int} = 45 bar, the equilibrium

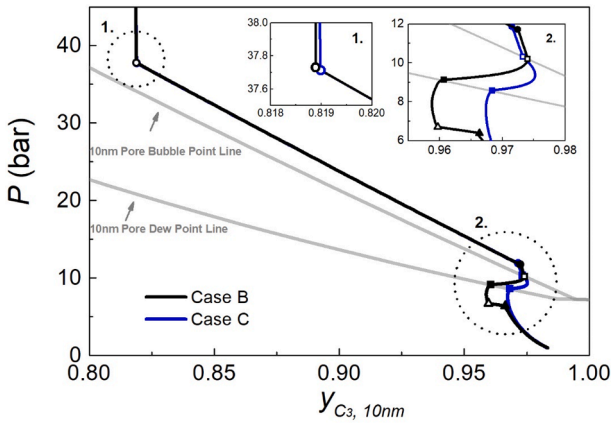

Fig. 4. The equilibrium $y_{C_3,10nm}$ for **Case B** and **C** during the CCE process. The open circles represent P_b^{bub}, the solid circles represent P_b^{dew}, the open squares represent P_{10nm}^{bub}, the solid squares represent P_{10nm}^{dew}, the open triangles represent P_{5nm}^{bub}, and the solid triangles represent P_{5nm}^{dew}.

$y_{C_3,b}$ in different cases are same. As P decreases, comparing to **Case B** and **C**, the molar fraction of C_3 in fluids released from the nanopores to the bulk region in **Case A** is smaller, resulting in a lower $y_{C_3,b}$ and a higher P_b^{bub}. At P belowP_b^{bub}, fluids in bulk region split into vapor and liquid two phases. Fluid properties in bulk vapor–liquid two phases are the same, while the molar ratio of vapor and liquid phases in bulk varies among different cases. The nanoconfinement effect in **Case A** is stronger compared with **Case B** and **C**. The stronger competitive adsorption in nanopores induces a smaller increase in the bulk vapor phase molar fraction. Since the bulk vapor-phase contains less C_3 compared to the bulk liquid-phase, a higher $y_{C_3,b}$ and a lower P_b^{dew} is observed in **Case A**. The equilibrium $y_{C_3,b}$ increases until $P < P_b^{dew}$. When phase transition occurs in nanopores, $y_{C_3,b}$ decreases in different cases. When a given nanopore is in vapor–liquid two-phase in different cases, vapor and liquid phases coexist with equal chemical potentials as proposed by Evans *et al.* [57], the equilibrium $y_{C_3,b}$ is the same. For multi-scale system with PSD effect, $y_{C_3,b}$ decreases continuously as P declines due to the continuous phase transitions from the larger pores to the smaller pores.

In Fig. 4, we present the equilibrium composition of C_3 in 10-nm pores, $y_{C_3,10nm}$, for **Case B** and **C**. When $P > P_b^{bub}$, the equilibrium $y_{C_3,10nm}$ increases more in **Case C** than **Case B** as P decreases. The molar fraction of C_3 in fluids released from the nanopores to the bulk region in **Case C** is larger, which increases C_3 concentration in the bulk region in **Case C**. Based on chemical potential equilibrium between nanopore and bulk, the equilibrium $y_{C_3,10nm}$ in **Case C** is higher than that in **Case B**. For $P_b^{bub} > P > P_b^{dew}$, $y_{C_3,10nm}$ are the same in **Case B** and **C** due to the same liquid phase properties in bulk. As P further decreases below P_b^{dew}, phase transition first occurs in the 10-nm pores, and the equilibrium $y_{C_3,10nm}$ decreases more in **Case B** than **Case C** as P decreases. As fluids in 10-nm pores split into liquid–vapor two phases, the properties of vapor and liquid two phases are the same in **Case B** and **Case C**. However, the volume fractions of those two phases are different due to different volume ratios of pores and bulk. Within the two-phase region of 10-nm pores, liquid phase density increases, while its volume decreases as$P$decreases [20]. The competition between density and volume causes the different trends in equilibrium $y_{C_3,10nm}$ in **Case B** and **C**. After the fluids in 10-nm pores completely vaporize, phase transitions can occur in 5-nm pores for **Case B**, and as fluids vaporize in 5-nm pores, $y_{C_3,10nm}$ increases in 10-nm pores. It is because the chemical potential of C_3 in bulk, which is equal to the liquid-phase chemical potential of C_3 in 5-nm pores, increases as P decreases within the 5-nm pores two-phase region. Such phenomena also affects the fluid properties in 10-nm pores as molar fraction of C_3 in them increases. On the other hand, the equilibrium compositions of C_3 in 5-nm pores, $y_{C_3,5nm}$, for **Case A** and **B**, are shown in Fig. 5. For **Case B**, the equilibrium $y_{C_3,5nm}$ increases as P decreases when phase transition occurs in the 10-nm pores due to the interplay between nanopores and bulk, which suppresses the phase transitions (both P_{5nm}^{bub} and P_{5nm}^{dew}) in 5-nm pores. In contrast to **Case A**, both P_{5nm}^{bub} and P_{5nm}^{dew} are lower in **Case B**.

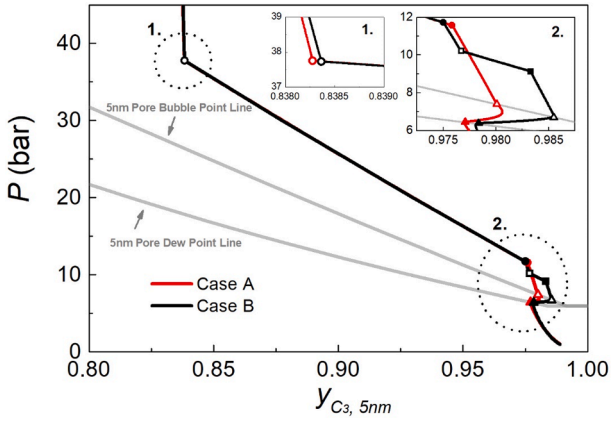

Fig. 5. The equilibrium $y_{C_3,5nm}$ for **Case A** and **B** during the CCE process. The open circles represent P_b^{bub}, the solid circles represent P_b^{dew}, the open squares represent P_{10nm}^{bub}, the solid squares represent P_{10nm}^{dew}, the open triangles represent P_{5nm}^{bub}, and the solid triangles represent P_{5nm}^{dew}.

In Fig. 6, we summarize the equilibrium C_3 composition in bulk, 10-nm and 5-nm pores when phase transitions occur in **Case B**. Within the bulk vapor–liquid two phases region, C_3 composition in bulk region decreases while those in 10-nm and 5-nm pores increase as P declines. It is because the competitive adsorption enhances the composition of the heavier component in nanopores as shown in Figs. 4 and 5. When $P_{10nm}^{dew} \leqslant P \leqslant P_{10nm}^{bub}$, C_3 composition in 10-nm pores decreases, while those in bulk and 5-nm pore increases. When $P_{5nm}^{dew} \leqslant P \leqslant P_{5nm}^{bub}$, C_3 compositions in bulk and 10-nm pores increases, while that in 5-nm pores decreases. Thanks to the stronger confinement effect in the smaller pores as well as the heavier component accumulation induced by interplay between nanopores and bulk, phase transition in the smaller pores occurs at lower pressures in shale multi-scale system. Overall, in the multi-scale system with PSD effect, when phase transition occurs in one specific region (bulk, 10-nm or 5-nm pores), the heavier component composition in this region decreases, while those in other regions increase. This interplay effect is in line with nanofluidic experiments by Wang *et al.* [16] and Jatukaran *et al.* [58].

In Fig. 7, we present the ratio of molar percentage of C_3 in bulk to that in the total system for **Case A**, **B** and **C**. The effect from different PSD becomes significant when pressure is below P_b^{dew}, which is also the main pressure range when C_3 can be released from nanopores. The higher volume ratio of the smaller pores in the system suppresses C_3 release process to a lower pressure condition and results in the smaller percentage of C_3 in the bulk region. It is because not only the effect of fluid-surface interaction becomes stronger as pore size decreases, but also the heavier component accumulates in the smaller pores when phase transition occurs in the larger pores. Overall, C_3 adsorbed into nanopores within bulk vapor–liquid coexist region due to competitive adsorption while it released from nanopore to outside bulk when bulk fluids in single phase, especially when phase transition happens in nanopores. Compared to C_3, C_1 can be continuously released from the nanopores to the bulk region for the entire pressure range as shown in **Fig. S5** (**Supplementary Information**).

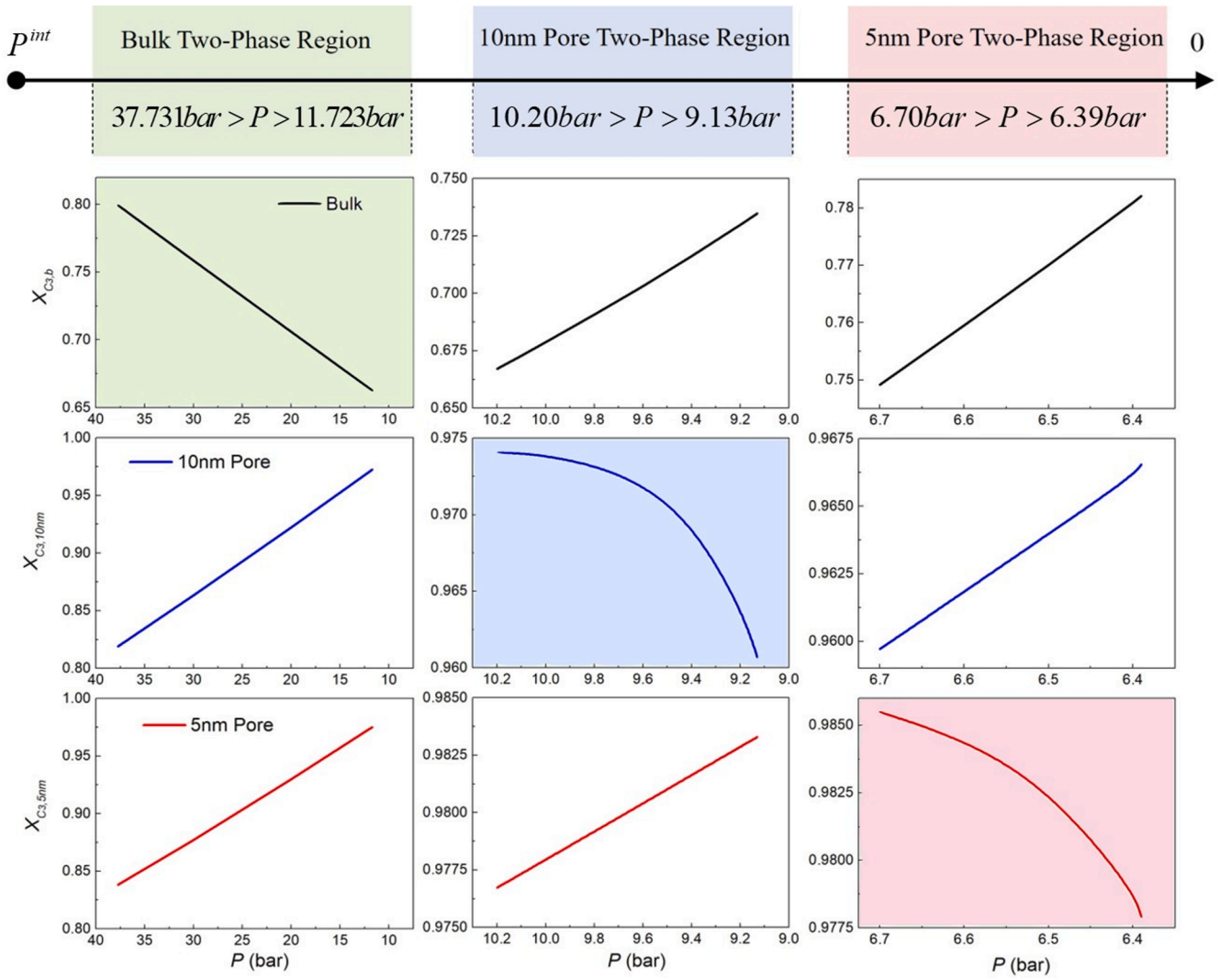

Fig. 6. The equilibrium y_{C_3} in bulk, 10 nm and 5 nm pores when phase transitions happen in **Case B**.

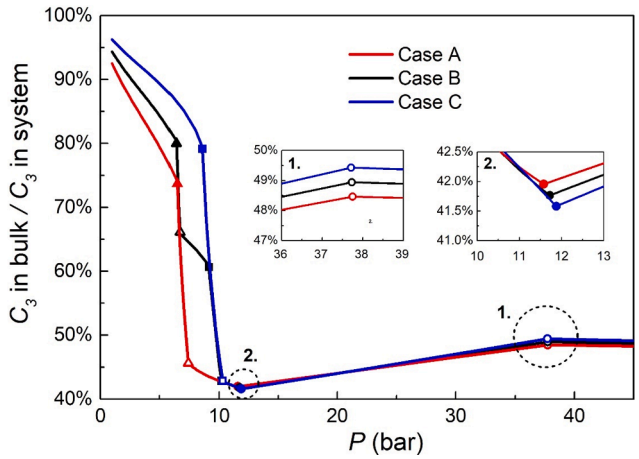

Fig. 7. Ratio of molar percentage of C_3 in bulk to that in total system for **Case A**, **B**, and **C** during the CCE process. The open circles represent P_b^{bub}, the solid circles represent P_b^{dew}, the open squares represent P_{10nm}^{bub}, the solid squares represent P_{10nm}^{dew}, the open triangles represent P_{5nm}^{bub}, and the solid triangles represent P_{5nm}^{dew}.

3.2. CVD

Fig. 8 presents the schematic diagram for phase transitions occuring in **Case B** during the CVD process at 288.15 K. Similar to the CCE process, phase transitions occur in the multi-scale system following the sequence of bulk, larger pores, smaller pores as P declines. Different from CCE, C_1-C_3 mixtures in excess volume is depleted to keep the volume of bulk recover back to V_b^i as Pdecreases. Due to competitive adsorption in nanopores, the depleted fluids in bulk region has a lower C_3 composition compared to the overall C_3 composition in the system. As a result, the remaining fluids in the total system become heavier as pressure drops. The heavier fluids in the system lead to instantaneous phase transitions in nanopores as shown in Fig. 8**f** and **h**.

In Fig. 9, we present the equilibrium $y_{C_3,b}$ for different cases in CVD process. When $P > P_b^{bub}$, the expanded bulk volumes in the CVD process recover back to V_b^i by depleting excess volume of pure liquid fluids in the bulk region. The nanoconfinement effect on the bulk fluid properties is stronger in CVD process compared to CCE, which leads to a lower bulk C_3 composition and a slightly higher P_b^{bub}. However, the difference between P_b^{bub} from CCE and CVD processes is negligible due to the small liquid phase volume expansion in bulk. For $P_b^{bub} > P > P_b^{dew}$, the bulk region begins to vaporize and a bulk vapor-phase emerges. The vapor phase in the bulk liquid–vapor two phases is depleted from the system, which alters the composition of remaining bulk fluids. As pressure

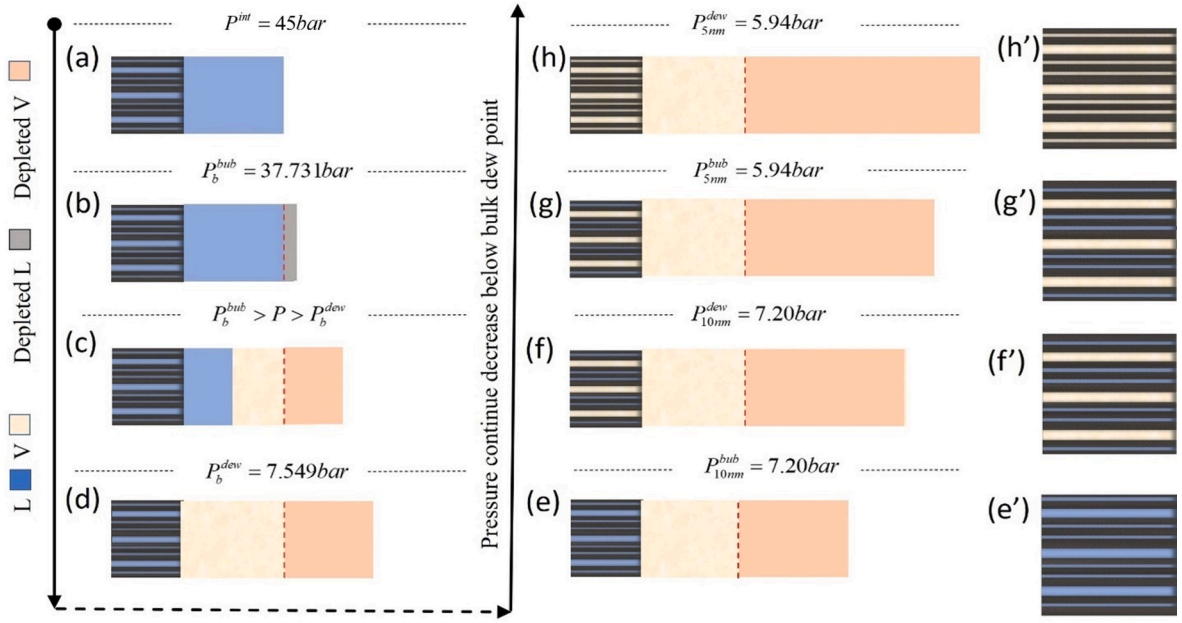

Fig. 8. .The schematic diagram for phase transitions in **Case B** during the CVD process at 288.15 K. (a) P^{int} = 45bar; (b) P_b^{bub} = 37.731bar; (c)$P_b^{dew} > P > P_{10nm}^{bub}$; (d) P_b^{dew} = 7.549bar; (e)P_{10nm}^{bub} = 7.20bar; (f) P_{10nm}^{dew} = 7.20bar; (g) P_{5nm}^{bub} = 5.94bar; (h) P_{5nm}^{dew} = 5.94bar. (e'); (f'); (g'); (h') are enlarged parts for nanopores in (e); (f); (g); (h) respectively. The blue color represents C_1/C_3 mixture in liquid phase while the yellow color represents vapor phase remained in nanopores or bulk region after depleting process. The gray color represents depleted C_1/C_3 mixture in liquid phase while the orange color represents depleted vapor phase in bulk region after excess volume depletion. The red dashed line provides a reference for the volume of bulk at initial condition. (For interpretation of the references to color in this figure legend, the reader is referred to the web version of this article.)

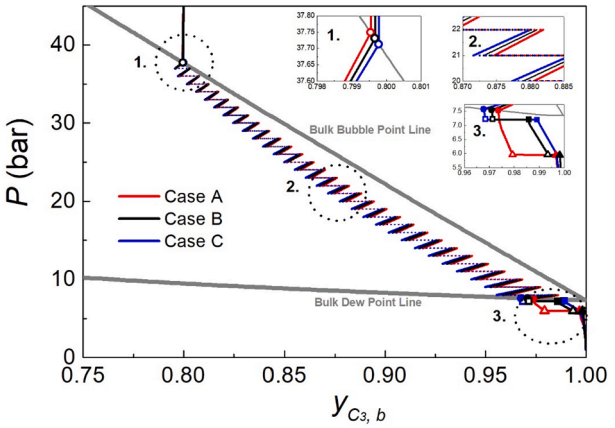

Fig. 9. The equilibrium $y_{C_3,b}$ for **Case A**, **B**, and **C** during the CVD process. The open circles represent P_b^{bub}, the solid circles represent P_b^{dew}, the open squares represent P_{10nm}^{bub}, the solid squares represent P_{10nm}^{dew}, the open triangles represent P_{5nm}^{bub}, and the solid triangles represent P_{5nm}^{dew}. In subfigure 2, the solid lines represent one stage of pressure decrease, the dotted lines represent one stage of excess volume depletion process.

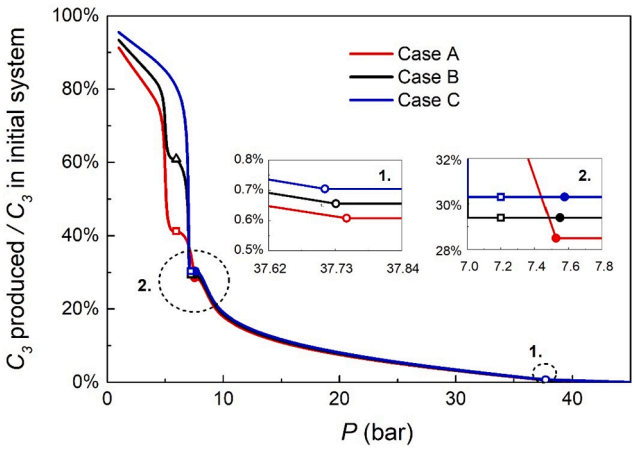

Fig. 10. Ratio of molar percentage of produced C_3 to that in total system for **Case A**, **B**, and **C** during the CVD process. The open circles represent P_b^{bub}, the solid circles represent P_b^{dew}, the open squares represent P_{10nm}^{bub}, the solid squares represent P_{10nm}^{dew}, the open triangles represent P_{5nm}^{bub}, and the solid triangles represent P_{5nm}^{dew}.

decreases, because C_3 is adsorbed into the nanopores, the equilibrium C_3 composition in the bulk region decreases. Then, the C_3 composition in bulk increases due to the excess bulk vapor-phase depletion. Overall, the effect of depletion is stronger than that of adsorption. Bulk C_3 composition keeps increasing during the CVD process, which decreases P_b^{dew} compared to the CCE process. Further decreasing P belowP_b^{dew}, phase transition occurs instantaneously in nanopores following the sequence of pore size from large to small. The change of equilibrium composition of C_3 in 10-nm pores and 5-nm pores, $y_{C_3,10nm}$ and $y_{C_3,5nm}$, are similar to the CCE process.

The ratio of molar percentage of produced C_3 to that in the initial system during the CVD process in different systems are shown in Fig. 10.

The release of the C_1/C_3 mixture shifts from the larger pores to the smaller pores. Recently, Li *et al.* [59] and Ma *et al.* [60] observed a similar phenomenon during CO_2 huff-n-puff and they claimed that the oil from the smaller pores is hard to be produced. Only around 30% of C_3 in the initial system could be produced until P decreases to P_b^{dew}. More than 60% of C_3 are produced when $P < P_b^{dew}$, which is the pressure range when the effect of PSD becomes significant. The higher volume ratio of the smaller pores in the system suppresses C_3 production process.

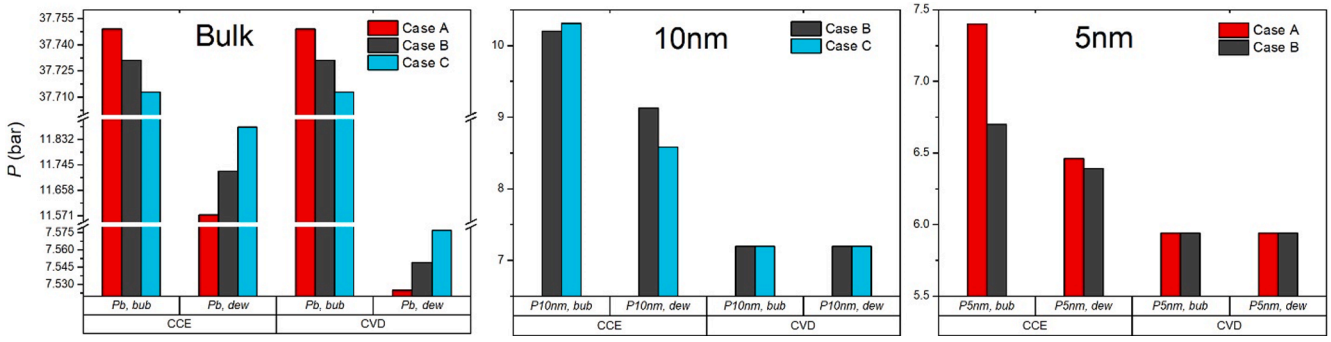

Fig. 11. The bubble point and dew point in bulk, 10-nm pores, and 5-nm pores during CCE and CVD processes for **Case A, B and C.**

3.3. Bubble point and dew point pressures

In Fig. 11, we summarize P_b^{bub}, P_b^{dew}, P_p^{bub}, P_p^{dew} in different nanopore-bulk multi-scale systems during the CCE and CVD process. The higher volume ratio of the smaller pores in the system results in a higher P_b^{bub} and a lower P_b^{dew}. As a result, the bulk two-phase region expands from **Case C** to **Case A**. The bulk two-phase regions in CVD process are larger than those in CCE process due to the lower P_b^{dew}, which is caused by keep depleting lighter component in excess volume depleting process. For nanopores, the breadths of vapor–liquid two phases regions are relatively narrow and mainly influenced by the volume ratio of bulk and nanopores [20]. In CCE process, the phase transition in 10-nm pores occurs at a higher pressure in the PSD model compared to the uniform pore size model. Under PSD effect, the phase transition in the smaller pores occurs at a lower condition compared to the uniform pore size case due to the heavier component accumulation. For CVD process, depleting lighter component from the total system further narrows the breadth of two-phase region in nanopores. In fact, the C_1-C_3 mixtures in nanopores become almost pure C_3, which leads to instantaneous phase transitions. Due to the PSD in shale media, phase transitions in the shale multi-scale system is a continuous process which cannot be described by a specific phase diagram by general EOS based methods.

4. Conclusion

In this work, we simultaneously consider the effect of fluid-surface interaction, interplay between nanopores and macropores/fractures, PSD inherent in shale media to investigate phase behaviors of C_1/C_3 mixture during CCE and CVD processes.

For both CCE and CVD processes, under the PSD effect, fluid phase transitions occur in the sequence of bulk, the larger pores, and the smaller pores, as pressure declines. When phase transition occurs in one specific region (bulk, 10-nm or 5-nm pores), the heavier component composition in this region decreases, while those in other regions increase. The effects of PSD become obvious when $P < P_b^{dew}$, which is also the main pressure range when C_3 can be released from the nanopores. In the CVD process, more than 60% of C_3 are produced when $P < P_b^{dew}$. Overall, the higher volume ratio of the smaller pores in the system suppresses the heavier component production process. This is not only because of the stronger confinement effect in the smaller pores, but also the heavier component accumulation induced by interplay between nanopores and bulk.

For bubble point and dew point in bulk, $P_b^{bub}$and P_b^{dew}, when the volume fraction of the smaller pores in the system is higher, P_b^{bub} is higher, while P_b^{dew} is lower, leading to an expanded bulk two-phase region. Compared with CCE process, the bulk two-phase regions in CVD process are larger due to a lower P_b^{dew}. For two-phase regions in nanopores, in CCE process, for a given nanopore, two-phase region expands as the volume ratio of pores to the initial bulk region increases [20]. In CVD process, phase transitions happen instantaneously in nanopores at a lower pressure condition compared to CCE process. It is because with lighter component depleted from the entire system, the heavier component composition in pores is higher and the C_1/C_3 mixture in nanopores becomes predominantly as pure C_3.

Our findings are also in line with the nanofluidic measurements for ternary hydrocarbon mixtures [58]. Model two-component systems (synthetic fluids) which are in the same homologous series as the multi-component systems (actual shale oil) have been widely used to study the underlying mechanisms of phase behaviors [61]. Thus, we believe that our work can provide important insights into hydrocarbon mixture phase behavior in shale formations. Based on thorough understandings about the phase behaviors in multi-scale shale matrix, this work evaluates the PSD effect on hydrocarbon thermodynamic properties and productions in shale matrix, which is imperative for the accurate prediction of well productivity, ultimate oil recovery and future EOR consideration.

CRediT authorship contribution statement

Yinuo Zhao: Methodology, Software, Validation, Formal analysis, Investigation, Writing - original draft, Visualization. **Zhehui Jin:** Conceptualization, Formal analysis, Investigation, Resources, Supervision, Funding acquisition.

Declaration of Competing Interest

The authors declare that they have no known competing financial interests or personal relationships that could have appeared to influence the work reported in this paper.

Acknowledgements

This research was enabled in part by support provided by Westgrid (www.westgrid.ca) and Compute Canada (www.computecanada.ca). The authors also greatly acknowledge a Discovery Grant from Natural Sciences and Engineering Research Council of Canada (NSERC RGPIN-2017-05080). As a part of the University of Alberta's Future Energy Systems research initiative, this research was made possible in part thanks to funding from the Canada First Research Excellence Fund.

Appendix A. Supplementary data

Supplementary data to this article can be found online at https://doi.org/10.1016/j.fuel.2021.120141.

References

[1] Zou C. Chapter 1 - Introduction. In: Zou C, editor. Unconventional Petroleum Geology (Second Edition). Elsevier; 2017. p. 3–48.
[2] Patade VY, Meher LC, Grover A, Gupta SM, Nasim M. Chapter 18 - Omics Approaches in Biofuel Technologies: Toward Cost Effective, Eco-Friendly, and

Renewable Energy. In: Barh D, Azevedo V, editors. Omics Technologies and Bio-Engineering. Academic Press; 2018. p. 337–51.
[3] J. Donnelly Comments: The Implications of Shale. SPE-1010-0018-JPT 2010;62 (10):18-.
[4] Ross DJK, Marc BR. The importance of shale composition and pore structure upon gas storage potential of shale gas reservoirs. Mar Pet Geol 2009;26(6):916–27.
[5] Didar BR, Akkutlu IY. Pore-size Dependence of Fluid Phase Behavior and Properties in Organic-Rich Shale Reservoirs. SPE International Symposium on Oilfield Chemistry. The Woodlands, Texas, USA: Society of Petroleum Engineers; 2013:19.
[6] Luo S, Lutkenhaus JL, Nasrabadi H. Use of differential scanning calorimetry to study phase behavior of hydrocarbon mixtures in nano-scale porous media. J Petrol Sci Eng 2018;163:731–8.
[7] Nojabaei B, Johns RT, Chu L. Effect of Capillary Pressure on Fluid Density and Phase Behavior in Tight Rocks and Shales. SPE-159258-MS 2012;16(3):281–9.
[8] Nguyen NTB, Dang CTQ, Chen Z, Nghiem LX. Optimization of Hydraulic Fracturing Design with Future EOR Considerations in Shale Oil Reservoirs. EUROPEC 2015. Madrid, Spain: Society of Petroleum Engineers; 2015:20.
[9] Zhao Y, Wang Y, Zhong J, Xu Y, Sinton D, Jin Z. Bubble Point Pressures of Hydrocarbon Mixtures in Multiscale Volumes from Density Functional Theory. Langmuir 2018;34(46):14058–68.
[10] Zhong J, Zhao Y, Lu C, Xu Y, Jin Z, Mostowfi F, et al. Nanoscale Phase Measurement for the Shale Challenge: Multicomponent Fluids in Multiscale Volumes. Langmuir 2018;34(34):9927–35.
[11] Qiu X, Tan SP, Dejam M, Adidharma H. Experimental Study on the Criticality of a Methane/Ethane Mixture Confined in Nanoporous Media. Langmuir 2019;35(36): 11635–42.
[12] Pathak M, Cho H, Deo M. Experimental and Molecular Modeling Study of Bubble Points of Hydrocarbon Mixtures in Nanoporous Media. Energy Fuels 2017;31(4): 3427–35.
[13] Cho H, Caputo D, Bartl MH, Deo M. Measurements of hydrocarbon bubble points in synthesized mesoporous siliceous monoliths. Chem Eng Sci 2018;177:481–90.
[14] Cho H, Bartl MH, Deo M. Bubble Point Measurements of Hydrocarbon Mixtures in Mesoporous Media. Energy Fuels 2017;31(4):3436–44.
[15] Liu Y, Li HA, Okuno R. Phase behavior of N2/n-C4H10 in a partially confined space derived from shale sample. J Petrol Sci Eng 2018;160:442–51.
[16] Wang L, Parsa E, Gao Y, Ok JT, Neeves K, Yin X, et al. Experimental Study and Modeling of the Effect of Nanoconfinement on Hydrocarbon Phase Behavior in Unconventional Reservoirs. SPE Western North American and Rocky Mountain Joint Meeting. Denver, Colorado: Society of Petroleum Engineers; 2014.
[17] Alfi M, Nasrabadi H, Banerjee D. Effect of Confinement on Bubble Point Temperature Shift of Hydrocarbon Mixtures: Experimental Investigation Using Nanofluidic Devices. San Antonio, Texas, USA: Society of Petroleum Engineers; 2017:12..
[18] Luo S, Lutkenhaus JL, Nasrabadi H. Multiscale Fluid-Phase-Behavior Simulation in Shale Reservoirs Using a Pore-Size-Dependent Equation of State. SPE-159258-MS 2018;21(04):806–20.
[19] Bi R, Nasrabadi H. Molecular simulation of the constant composition expansion experiment in shale multi-scale systems. Fluid Phase Equilib 2019;495:59–68.
[20] Zhao Y, Jin Z. Hydrocarbon-Phase Behaviors in Shale Nanopore/Fracture Model: Multiscale, Multicomponent, and Multiphase. SPE J 2019;24(6):2524–40.
[21] Tripathy A, Srinivasan V, Singh TN. A Comparative Study on the Pore Size Distribution of Different Indian Shale Gas Reservoirs for Gas Production and Potential CO2 Sequestration. Energy Fuels 2018;32(3):3322–34.
[22] Clarkson CR, Freeman M, He L, Agamalian M, Melnichenko YB, Mastalerz M, et al. Characterization of tight gas reservoir pore structure using USANS/SANS and gas adsorption analysis. Fuel 2012;95:371–85.
[23] Clarkson CR, Solano N, Bustin RM, Bustin AMM, Chalmers GRL, He L, et al. Pore structure characterization of North American shale gas reservoirs using USANS/SANS, gas adsorption, and mercury intrusion. Fuel 2013;103:606–16.
[24] Dong T, Harris NB, Ayranci K, Twemlow CE, Nassichuk BR. The impact of composition on pore throat size and permeability in high maturity shales: Middle and Upper Devonian Horn River Group, northeastern British Columbia, Canada. Mar Petrol Geol 2017;81:220–36.
[25] Hu Q, Ewing RP, Rowe HD. Low nanopore connectivity limits gas production in Barnett formation. J Geophys Res Solid Earth 2015;120(12):8073–87.
[26] Chen G, Lu S, Liu K, Xue Q, Xu C, Tian S, et al. Investigation of pore size effects on adsorption behavior of shale gas. Mar Pet Geol 2019;109:1–8.
[27] Jin L, Ma Y, Jamili A. Investigating The Effect of Pore Proximity on Phase Behavior And Fluid Properties in Shale Formations. New Orleans, Louisiana, USA: Society of Petroleum Engineers; 2013:16..
[28] Jin B, Bi R, Nasrabadi H. Molecular simulation of the pore size distribution effect on phase behavior of methane confined in nanopores. Fluid Phase Equilib 2017; 452:94–102.
[29] Liu Y, Ma X, Li HA, Hou J. Competitive adsorption behavior of hydrocarbon(s)/CO2 mixtures in a double-nanopore system using molecular simulations. Fuel 2019;252:612–21.
[30] Leu L, Georgiadis A, Blunt MJ, Busch A, Bertier P, Schweinar K, et al. Multiscale Description of Shale Pore Systems by Scanning SAXS and WAXS Microscopy. Energy Fuels 2016;30(12):10282–97.
[31] Boruah A, Rasheed A, Mendhe VA, Ganapathi S. Specific surface area and pore size distribution in gas shales of Raniganj Basin, India. J Pet Explor Prod Technol 2019; 9(2):1041–50.
[32] Wang L, Neeves K, Yin X, Ozkan E. Experimental Study and Modeling of the Effect of Pore Size Distribution on Hydrocarbon Phase Behavior in Nanopores. SPE Annual Technical Conference and Exhibition. Amsterdam, The Netherlands: Society of Petroleum Engineers; 2014:15.
[33] Wang L, Yin X, Neeves KB, Ozkan E. Effect of Pore-Size Distribution on Phase Transition of Hydrocarbon Mixtures in Nanoporous Media. SPE J 2016;21(06): 1981–95.
[34] Luo S, Lutkenhaus JL, Nasrabadi H. Effect of Nano-Scale Pore Size Distribution on Fluid Phase Behavior of Gas IOR in Shale Reservoirs. SPE Improved Oil Recovery Conference. Tulsa, Oklahoma, USA: Society of Petroleum Engineers; 2018:14.
[35] Liu J, Wang L, Xi S, Asthagiri D, Chapman WG. Adsorption and Phase Behavior of Pure/Mixed Alkanes in Nanoslit Graphite Pores: An iSAFT Application. Langmuir 2017;33(42):11189–202.
[36] Pitakbunkate T, Balbuena PB, Moridis GJ, Blasingame TA. Effect of Confinement on Pressure/Volume/Temperature Properties of Hydrocarbons in Shale Reservoirs. SPE J 2016;21(2):621–34.
[37] Jin Z. Bubble/dew point and hysteresis of hydrocarbons in nanopores from molecular perspective. Fluid Phase Equilib 2018;458:177–85.
[38] Liu J, Zhao Y, Yang Y, Mei Q, Yang S, Wang C. Multicomponent Shale Oil Flow in Real Kerogen Structures via Molecular Dynamic Simulation. Energies 2020;13(15): 3815.
[39] Wang Y, Zhu Y, Chen S, Li W. Characteristics of the Nanoscale Pore Structure in Northwestern Hunan Shale Gas Reservoirs Using Field Emission Scanning Electron Microscopy, High-Pressure Mercury Intrusion, and Gas Adsorption. Energy Fuels 2014;28(2):945–55.
[40] Zhang Y, Shao D, Yan J, Jia X, Li Y, Yu P, et al. The pore size distribution and its relationship with shale gas capacity in organic-rich mudstone of Wufeng-Longmaxi Formations, Sichuan Basin, China. J Nat Gas Geosci 2016;(3):213–20.
[41] Liu Q, Xu B. Actuating Water Droplets on Graphene via Surface Wettability Gradients. Langmuir 2015;31(33):9070–5.
[42] Jagadisan A, Heidari Z. Impacts of Geochemical Properties on Wettability of Kerogen and Organic-rich Mudrocks. Unconventional Resources Technology Conference, Houston, Texas, 23-25 July 2018. Society of Exploration Geophysicists, American Association of Petroleum Geologists, Society of Petroleum Engineers; 2018, p. 3149-66.
[43] Jagadisan A, Heidari Z. Experimental Quantification of Kerogen Wettability as a Function of Thermal Maturity. London, UK: Society of Petrophysicists and Well-Log Analysts; 2018:14..
[44] Wang S, Zhang Y, Abidi N, Cabrales L. Wettability and Surface Free Energy of Graphene Films. Langmuir 2009;25(18):11078–81.
[45] Ho TA, Wang Y, Xiong Y, Criscenti LJ. Differential retention and release of CO2 and CH4 in kerogen nanopores: Implications for gas extraction and carbon sequestration. Fuel 2018;220:1–7.
[46] Wu T, Zhao H, Tesson S, Firoozabadi A. Absolute adsorption of light hydrocarbons and carbon dioxide in shale rock and isolated kerogen. Fuel 2019;235:855–67.
[47] Medeiros F, Kurtoglu B, Ozkan E, Kazemi H. Analysis of Production Data From Hydraulically Fractured Horizontal Wells in Shale Reservoirs. SPE-159258-MS 2010;13(03):559–68.
[48] Fan L, Thompson JW, Robinson JR. Understanding Gas Production Mechanism and Effectiveness of Well Stimulation in the Haynesville Shale Through Reservoir Simulation. Canadian Unconventional Resources and International Petroleum Conference. Calgary, Alberta, Canada: Society of Petroleum Engineers; 2010:15.
[49] Sigal RF. Pore-Size Distributions for Organic-Shale-Reservoir Rocks From Nuclear-Magnetic-Resonance Spectra Combined With Adsorption Measurements. SPE J 2015;20(4):824–30.
[50] Ko LT, Loucks RG, Ruppel SC, Zhang T, Peng S. Origin and characterization of Eagle Ford pore networks in the south Texas Upper Cretaceous shelf. AAPG Bull 2017;101(3):387–418.
[51] Peng D-Y, Robinson DB. A New Two-Constant Equation of State. Ind Eng Chem Fundam 1976;15(1):59–64.
[52] Ravikovitch PI, Domhnaill SCO, Neimark AV, Schueth F, Unger KK. Capillary Hysteresis in Nanopores: Theoretical and Experimental Studies of Nitrogen Adsorption on MCM-41. Langmuir 1995;11(12):4765–72.
[53] Firoozabadi A. Thermodynamics and Applications of Hydrocarbons Energy Production. McGraw-Hill. Education 2015.
[54] C.H. Whitson T.SB. Evaluating Constant-Volume Depletion Data. 35 03 SPE-1010-0018-JPT 1983, 610 620.
[55] Behnous D, Zeraibi N, Belgacem D. Study of Gas Condensate Reservoir Behaviour using PVT Experiment; 2017.
[56] Freeman C, Moridis GJ, Michael GE, Blasingame TA. Measurement, Modeling, and Diagnostics of Flowing Gas Composition Changes in Shale Gas Wells. SPE Latin America and Caribbean Petroleum Engineering Conference. Mexico City, Mexico: Society of Petroleum Engineers; 2012:25.
[57] Evans R, Marconi UMB, Tarazona P. Fluids in narrow pores: Adsorption, capillary condensation, and critical points. J Chem Phys 1986;84(4):2376–99.
[58] Jatukaran A, Zhong J, Abedini A, Sherbatian A, Zhao Y, Jin Z, et al. Natural gas vaporization in a nanoscale throat connected model of shale: multi-scale, multi-component and multi-phase. Lab Chip 2019;19(2):272–80.
[59] Li L, Wang C, Li D, Fu J, Su Y, Lv Y. Experimental investigation of shale oil recovery from Qianjiang core samples by the CO2 huff-n-puff EOR method. RSC Adv 2019;9 (49):28857–69.
[60] Ma Q, Yang S, Lv D, Wang M, Chen J, Kou G, et al. Experimental investigation on the influence factors and oil production distribution in different pore sizes during CO2 huff-n-puff in an ultra-high-pressure tight oil reservoir. J Petrol Sci Eng 2019; 178:1155–63.
[61] McCain Jr WD. Properties of petroleum fluids. PennWell Corporation 2017.